Quantitative Analysis of trace levels of surface contamination by X-ray photoelectron spectroscopy
Part II: Systematic uncertainties and absolute quantification

Nadir S. Faradzhev,* Shannon B. Hill, and Cedric J. Powell

National Institute of Standards and Technology, Gaithersburg, MD 20899

ABSTRACT

We discuss analyses of trace levels of surface contamination using X-ray photoelectron spectroscopy (XPS). The problem of quantifying common sources of statistical and systematic uncertainties for these measurements is formulated in terms of the needs of extreme ultraviolet (EUV) lithography, but the results and conclusions are applicable to a broad range of XPS applications. We quantify the systematic uncertainties introduced by particular cases of overlapping peaks on different substrate structures by simulating measured spectra with the National Institute of Standards and Technology Database for the Simulation of Electron Spectra for Surface Analysis (SESSA). One example demonstrates that the relative atomic concentrations of trace elements such as S, P, and halogens on a Ru surface could be dramatically overestimated if the fitting of the overlapping Ru 3d and C 1s peaks excludes the contribution from carbon. We also show how spectra generated by SESSA can be compared with measured spectra to determine absolute amounts of surface impurities on layered samples of the type used for EUV lithography. We provide estimates of the total uncertainty for such measurements by considering the systematic limitations of SESSA and the statistical uncertainties of the measurements. The same procedure can be employed for other multilayered materials. Finally, we describe two approaches for converting XPS detection limits for an elemental impurity in an elemental matrix to the corresponding detection limits for the impurity as a thin film on the surface of the matrix material.

Introduction

Detection and quantification of trace levels of surface contamination is a challenge for many modern analytical techniques. X-ray photoelectron spectroscopy (XPS) is widely used to obtain quantitative information about surface composition and the chemical states of elements in the near-surface region from which the signals originate. Industrial laboratories utilize XPS to

* Current affiliation: KLA Tencor, 3 Technology Drive, Milpitas, CA 95035; email: nadir.faradzhev@kla-tencor.com

evaluate the type and amount of surface contamination in applications for which the X-ray flux does not cause significant modification of the sample surface during analysis. Our work was motivated by one such industrial application that, until recently, was used to qualify resists for use in extreme ultraviolet (EUV) lithography scanners.[1] High fluxes of energetic EUV photons (13.5 nm) combined with the outgassing from photoresists can damage EUV optics.[2] As a result, every newly formulated EUV photoresist was assessed by exposing a witness-sample to its outgas products. XPS was used in the final step of these tests to detect and quantify trace levels of metals, non-metals, and halogens. This information could be used to estimate potentially irreversible reflection losses of EUV optics associated with the given resist.[3]

In Part 1 of this work,[4] we described the statistical uncertainties associated with measurements of arbitrary species present on a surface at trace levels. In Part 2, we focus on the specific case of submonolayer coverages of selected nonmetals (N, S, P) and halogens (F, Cl, Br) on thick Ru witness samples used in EUV lithography resist-outgas tests. We discuss uncertainties in the amounts of surface impurities that arise from simplifying assumptions often made in quantitative XPS of multilayered samples. This discussion is based on simulated XPS spectra using the National Institute of Standards and Technology (NIST) Database for the Simulation of Electron Spectra for Surface Analysis (SESSA).[5,6] We first consider the effects of carbonaceous contamination on the quantification of other surface impurities. We show that the impurity amount can be significantly overestimated if the intensity of the Ru 3d photoelectron peak is determined without separating the overlapping C 1s peak. Second, we illustrate how SESSA can be used to convert measured photoelectron intensities from surface impurities into absolute amounts of trace elements on a surface. While the latter simulations are specific to our witness samples, the methodology is of general utility. Finally, we propose two methods for converting XPS detection limits for an elemental impurity in an elemental matrix to the corresponding detection limits for the corresponding impurity as a thin film on the surface of the matrix material.

Experiments and simulations

We consider two types of witness samples used for EUV resist-outgassing tests. We study the impact of overlapping peaks on the quantification of trace elements on a thick Ru layer (comprised of >30 nm of Ru on a Si substrate), and we compare measured and simulated spectra to estimate absolute amounts of impurities on both thick Ru layers and on multilayer mirror (MLM) samples of the type used for EUV optics[7]. The latter consisted of about 50 Si/Mo bi-layers, each 6.7 nm thick, on a Si substrate (Figure 1). The top bilayer was coated with a 1 nm to 2 nm polycrystalline Ru capping layer to protect the optics from EUV-induced oxidation. According to

our XPS measurements, the top-most surface of the Ru on both sample types was a native oxide ($RuO_{x\cong2}$; ≈ 0.5 nm thick), in agreement with earlier studies.[8]

XPS measurements were made with a commercial Kratos Axis Ultra spectrometer.[9] All spectra were obtained with a monochromatic Al Kα x-ray source (operated at 140 W) and with the analyzer operated in the immersion magnetic lens mode with 80 eV pass energy. (Although a pass energy of 160 eV would have provided better signal-to-noise, 80 eV was selected as a compromise between sensitivity and adequate energy resolution for fitting of overlapping peaks.) The angle between the energy analyzer and the x-ray source was fixed at 60°, and the analyzer acceptance semi-angle was 15°. Two different emission angles were used as described below. The energy step size was 1 eV for the survey spectra and 0.2 eV for the narrow scans of a single peak.

Our SESSA[5,6] simulations were performed with instrumental settings corresponding to those of our XPS instrument. Simulations of EUV multilayer optics were made with typically a single Si/Mo bilayer on a Si substrate that was covered by the Ru/RuO_2 capping layer (since the information depth corresponding to 95 % of a peak intensity in our XPS measurements was estimated to be less than 9 nm).[10] Finally, varying amounts of selected surface impurities (N, S, P, or halogens) were included together with a thin film of carbon that represented hydrocarbons that are typically adsorbed on the EUV optics after exposure to air. The amounts of material in particular layers for a SESSA simulation are specified by film thicknesses. We note that film thicknesses less than atomic dimensions are clearly unphysical but are used here to indicate the equivalent amounts of material in the film (as fractional monolayers) that are needed to give particular peak intensities. In such cases, we present film thicknesses in monolayer (ML) units where a ML thickness is defined as twice the van der Waals radius of a given atom.[11] The latter choice provides useful estimates of film thicknesses but the values are believed to be lower limits.

Results

Core-level electrons excited by X-ray photons deliver quantitative information about the species in a thin surface region.[10] The measured intensity for a particular peak is determined by the number of electrons in the relevant subshell, the photoionization cross section, the depth distribution of analyzed atoms, elastic- and inelastic-scattering processes in each layer, possible structural and chemical effects, the measurement configuration, the analyzer acceptance angle, and the efficiency of the detector.[10] In practice, however, estimates of the surface composition are often made using a number of simplifying assumptions. First, the sample of interest is assumed to be homogeneous within the XPS information depth. Second, no account is taken of matrix effects associated with corrections for different atomic densities, different inelastic mean

free paths, and different elastic-scattering effects in the sample of interest and a selected reference material.[10] Third, intensity modulations associated with possible structural ordering are neglected. Finally, possible intensity variations due to a change of chemical state (e.g., due to shakeup) are also neglected.[10] The relative concentration of the i-th species in the surface region, C_i, can then be expressed as

$$C_i = \frac{I_i/R_i}{\sum_j I_j/R_j}. \quad (1)$$

Here I_i is the intensity of the i-th peak and R_i is the elemental relative sensitivity factor for that particular species, energy level, and operation mode of the XPS instrument. As is common practice, I_i is taken to be the area of the spectral feature after subtraction of a suitable background and hence has units of counts per second times electron volts. [See Eq. (2) of Part 1.[4]]

Uncertainties resulting from analysis procedures for overlapping peaks

In this section, we discuss the uncertainties in atomic concentrations of surface impurities derived from overlapping peaks. We first note that Powell and Conny[12] showed how photoelectron peak intensities can vary from the different methods used for background subtraction and the various procedures chosen for setting integration limits. Conny *et al.*[13–15] also showed that the analysis of overlapping peaks of a doublet could be problematic if the peaks are relatively wide and their separation is small.

The uncertainties in derived elemental concentrations resulting from background-subtraction and peak-fitting procedures may become significant if the relative sensitivity factors for the overlapping peaks are very different. Indeed, detection and quantification of carbon on ruthenium is a challenge due to the much lower photoemission cross section of C 1s compared to that for the overlapping Ru 3d features. Together with the asymmetric line shapes of both transitions, the much lower sensitivity of C can lead to substantial uncertainty in an analysis if multiple-peak fitting models are employed to separate the C and Ru signals.[14] Because of this difficulty, some applications with low levels of C on Ru assume that the uncertainty arising from fitting the weak C 1s feature will be larger than the error introduced by ignoring the contribution from carbon. We will show that exclusion of carbon in commonly used methods for quantitative XPS leads to significant systematic biases in derived atomic concentrations of trace surface-impurity elements even for very thin carbon layers.

We used SESSA to simulate photoelectron spectra for a series of samples containing carbon and small quantities of other elements (S, P, or halogens) in the surface region. The substrate was a 30 nm Ru film covered with a 0.5 nm oxide layer (Figure 1). The objective of these simulations was not to predict atomic concentrations of real systems with high absolute accuracy. This would not be instructive due to the inherently large systematic uncertainty resulting from

fitting of multiple, overlapping, asymmetric peaks of different widths, especially for the low-energy resolution spectra studied here. Instead our goal is to demonstrate the general trends and relative differences between different analysis methods for a representative system. To that end, the shapes, widths and chemical shifts of the simulated Ru 3d and C 1s features were chosen to give reasonable qualitative agreement with the measured spectrum, not an exact match. Likewise, the observations discussed below are largely independent of the absolute accuracy of the relative sensitivity factors (e.g., 0.278 for C 1s and 4.27 for Ru $3d_{(5/2+3/2)}$ as provided by Kratos). Examples of total and component spectra calculated for the Ru 3d/C 1s region are shown in Figure 2 for a sample with 0.07 nm (0.19 ML) of S and 0.5 nm of C on the surface of RuO_2-covered Ru as indicated in the Figure caption. The simulations used the XPS configuration described above with the analyzer axis set to 50° with respect to the surface normal.

We see that the Ru $3d_{3/2}$ and the C 1s peaks associated with aliphatic carbon in Figure 2 nearly coincide. We have analyzed the total spectrum shown in Figure 2 for varying thicknesses of the surface C layer with commonly used methods of quantitative XPS analysis. First, the sample was assumed to be homogeneous over the XPS information depth. Second, we used the CasaXPS software[9,16] to fit regions of simulated spectra to obtain elemental signals. The Ru 3d/C 1s region was fitted using a Shirley background and the elemental signals were obtained using two different assumptions. For Assumption A, the contribution of C to the Ru 3d/C 1s intensity ratio was postulated to be non-negligible, and the fits were made using a Ru 3d doublet and a single C 1s peak. The resulting Ru and C peak areas were then used in the sum in the denominator of Eq. (1) to determine the atomic concentration of other species. For Assumption B, we assumed that the contribution of C to this region was very small and fitted the total envelope only with the Ru 3d doublet peaks; i.e., we assumed there was no C 1s peak contribution to the fits or in the application of Eq. (1). For both cases, the area ratio of the $3d_{5/2}$ and $3d_{3/2}$ components of the Ru 3d doublet was assumed to be 3:2, and the Ru 3d and C 1s peak positions were constrained within 10 % of the values used in the simulations. Figure 3 shows the relative atomic concentrations of S, derived using our two assumptions, as a function of the thickness of the C surface layer. These results are based on simulations similar to those shown in Figure 2 but for a fixed S film thickness of 0.07 nm (0.19 ML) between the RuO_2 and the C. Figure 3 indicates that that the derived S atomic concentrations (for the assumed homogeneous sample) depended strongly on whether we include or exclude the C 1s peak in the peak fits of the Ru 3d/C 1s region. The denominator in Eq. (1) can be much larger in the former case (Assumption A) because the C 1s peak area is normalized to the relative sensitivity factor for C 1s which is more than 10 times smaller than that for Ru 3d. Hence, when the C 1s peak is neglected and the entire area of the Ru 3d/C 1s region is attributed only to Ru (Assumption B), the S concentration can be overestimated by 50 % for C thicknesses as small as 0.25 nm and by more than a factor of two for C thicknesses greater than 0.75 nm.

Figure 4 shows the dependence of the derived atomic concentration of sulfur on the thickness of the sulfur layer based on our Assumptions A and B. We assumed that the outermost C layer had a fixed thickness of 0.5 nm. This C film represents the carbonaceous layer typically observed for air-exposed Ru samples. Figure 4 shows that the derived S concentration is proportional to the S thickness with different slopes for Assumption A and Assumption B (i.e., with or without, respectively, inclusion of the C 1s component in the fits to the Ru 3d/C 1s region). The horizontal dashed line indicates the critical S atomic concentration from XPS measurements designated as the upper limit for satisfactory performance of EUV mirrors.[1] The actual amount of S that results in a finding of a critical S concentration from an XPS analysis will thus vary by almost a factor of two depending on which assumption (A or B) is used in the data analysis.

To quantify the differences shown in Figure 4 we define the relative concentration difference δC_i for species i as the difference between the two absolute concentrations, $C_{i,A}$ and $C_{i,B}$, derived using Assumptions A and B, respectively, for the same amount of element i on the surface normalized to the average concentration $\left(C_{i,A} + C_{i,B}\right)/2$:

$$\delta C_i = \frac{C_{i,B} - C_{i,A}}{(C_{i,A} + C_{i,B})/2} = \frac{b_i - a_i}{(a_i + b_i)/2}. \quad (2)$$

Here, a_i and b_i are the slopes of the lines obtained from plotting $C_{i,A}$ and $C_{i,B}$, respectively, as a function of coverage of species i (e.g., Figure 4). From the slopes of the lines in Figure 4 for sulfur ($i = S$), δC_S =57 %. Similar analyses of SESSA simulations for surface impurities P, F, Br and Cl with atomic concentrations between 0.5 and 5 atomic percent produced δC_i values of 56 %, 50 %, 57 % and 42 %, respectively. For such small concentrations, δC_i is independent of the relative sensitivity factor of the impurity element, but it is very sensitive to the shape of the Ru 3d/C 1s region due to the inherent complexity of fitting multiple overlapping asymmetric peaks. This is why the δC_i are so similar for S, P, F and Br, which all have peaks far from the Ru 3d/C 1s region. δC_{Cl} is somewhat lower than the others because the peak fitting is perturbed by the overlap of the Cl $2p_{3/2}$ peak with the low-binding-energy tail of the Ru $3d_{5/2}$ peak.

Our results indicate that the derived relative atomic concentration of the trace element on the surface of Ru is always larger if the carbon peak is not included in fits of the Ru 3d/C 1s region. These differences could be critical in some applications, e.g., an EUV resist may be disqualified if the measured concentration of a contaminant species is determined to be above a certain threshold during a resist outgas test. In such cases, the procedure should specify whether the C 1s peak should be included in the analysis of the Ru 3d/C 1s region. Alternatively, the atomic concentration could be determined using the Ru 3p peak which does not overlap with the C 1s peak.

Absolute quantification of surface impurities

We have used SESSA to simulate XPS spectra of a thick Ru sample and a MLM EUV-optic sample, and have compared the simulated spectra with measured spectra. Our objective here is to determine the absolute amount of surface impurities on the test samples.

Our measured spectra showed weak peaks due to N, Cl, and F that typically arise from resist outgassing during EUV irradiation. For the resist-outgassing test protocols, such XPS spectra would be used to determine the atomic concentrations (using Eq. 1) of the trace elements which would then be compared to a prescribed maximum allowable value. This methodology is commonly employed by analysists in many fields and inherently assumes that the samples are homogeneous. There are two problems with this approach. First, the samples consist of multiple thin layers and are therefore not homogeneous. As a result, the derived amounts of impurities have no absolute significance. Second, it is difficult to compare such measures among different XPS laboratories, even as relative measures of surface composition, because of the use of different XPS instruments, different measurement conditions, and possibly different relative sensitivity factors.[10]

We present two examples of the use of SESSA for obtaining quantitative measures of the amounts of surface impurities on MLM samples. In our first example, Figure 5 shows a measured wide-scan XPS spectrum (solid blue circles) of a thick (> 30 nm) Ru film on a Si substrate which we designate here as Sample A. This spectrum shows weak peaks due to N and F as well as the expected peaks of Ru, C, and O (from the oxidized Ru). The solid red triangles in Figure 5 show a simulated spectrum for a sample consisting of an outermost 0.25 nm layer of $CN_{0.02}F_{0.02}$ on 0.25 nm C and 0.25 nm RuO_2 on a Ru substrate. The stoichiometry of the outermost layer is intended to indicate that both N and F were present in this layer as impurities.

Our simulations were performed for the same XPS configuration described above. For Sample A the analyzer axis was normal to the surface and the incidence angle of x rays on the sample was 60° with respect to the sample normal. We selected the photoionization cross sections of Scofield,[17] the dipole asymmetry parameters of Reilman *et al*.,[18] a differential inverse inelastic mean free path (DIIMFP) of Ru,[19] the inelastic mean free paths (IMFPs) of Tanuma *et al.*[20] for the elemental solids, and the TPP-2M IMFP predictive formula for RuO_2 and the $CN_{0.02}F_{0.02}$ layer.[21] We adjusted the widths of the major peaks in the simulated spectra to correspond to those in the measured spectra.

The simulated spectrum was multiplied by the transmission function for the operating conditions of the XPS instrument and then normalized to the measured spectrum at a binding energy of 390 eV. We see that the measured and simulated spectra in Figure 5 show major peaks due to Ru (with the C 1s peak overlapping the Ru $3d_{3/2}$ peak, as in Figure 2) and weaker peaks that are due to F, O, and N. A limitation of SESSA is that a user can select only one or two DIIMFPs

to describe the relative probabilities of inelastic scattering as a function of energy loss. We chose to use the Ru DIIMFP for all layers of the structure since Ru is the major constituent in the near-surface region (i.e., within one IMFP of the surface). This simplification resulted in faster simulations than if two DIIMFPs were selected.

While the measured and simulated spectra in Figure 5 are quite similar, there are some obvious differences. For example, the intensities of the simulated Ru photoelectron peaks are larger than the corresponding measured values, and the inelastic background associated predominantly with the Ru 3s and 3p peaks at binding energies between 600 eV and 800 eV is stronger in the simulated spectrum than in the measured spectrum. In addition, it was assumed, for simplicity, that the peak shapes were Lorentzian; as a result, the tails of the peaks do not match the experimental peak shapes. Finally, the SESSA simulations were performed with a single DIIMFP that does not provide a good match with the energy-loss features associated with the overlapping Ru 3d and C 1s peaks. Although Ru is the major constituent of the structure, the DIIMFP for Ru in SESSA provides only a rough description of the energy-loss features on the low-kinetic-energy side of each photoelectron peak in Figure 5. Despite the differences between the measured and simulated spectra in Figure 5, it is straightforward to quantify the amounts of N and F in this sample. It is sufficient for our purpose to recognize that the weak F and N peaks in Figure 5 originate from impurities, in this case in the outermost layer. As a result, the impurity peaks appear on the slowly varying inelastic backgrounds associated with the other constituent atoms. Relatively large changes in the assumed underlayer film thicknesses (up to 1 nm) merely change the simulated intensities of the major peaks and their inelastic backgrounds but have little effect on the simulated intensities of the N and F peaks. We therefore only need rough matches of the simulated and measured peak intensities and their associated inelastic backgrounds.

Figure 6 shows expanded views of the spectral regions in Figure 5 that contain the F 1s and N 1s peaks. There are no obvious inelastic features on the low-kinetic-energy sides of these peaks, as expected for surface impurities.[22,23] Simple linear backgrounds were assumed for both the F 1s and N 1s peaks. As described in Part 1 of this work,[4] the backgrounds were defined as the line connecting the mean endpoints determined by averaging equal numbers of background points on each side of the peak. As is common practice, half of these background points were also used to define the peak area. We call this commonly employed method of background determination "symmetric, semi-correlated endpoint averaging," and the statistical uncertainty of the background-subtracted area is given by Eq. (6) of Part 1 with $n_{SA} = n_S/2$. As described in Part 1, $n_S = N_S/N_P$, where N_S is the number of points on each side of the peak used to determine the background, and N_P is the number of points comprising only the peak (including no background points). Unless stated otherwise, we minimized the uncertainty by selecting, $N_S = N_P$ [As per Eq. (11) of Part 1]. Comparisons of the resulting peak areas from the measured and

simulated spectra indicated that the composition of the outermost 0.25 nm impurity layer is $CN_{0.053}F_{0.032}$. This result corresponds to effective coverages for N and F of 0.043 ML and 0.027 ML, respectively, where we have utilized van der Waals radii of 0.155 nm and 0.147 nm for N and F, respectively, to convert film thicknesses to estimate surface coverages.

The weak peaks identified as F 1s and N 1s in Figure 6 (a) and (b) consist of at most 7 points, only three or four of which are distinctly above the background. With $N_P = 7$ in Eq. (6) of Part 1, the estimated standard deviations in the determination of the F 1s and N 1s peak areas are relatively large at 19 % and 29 %, respectively. If more precise measures of the surface-impurity concentrations were needed, these could be obtained from higher-energy-resolution scans of the F 1s and N 1s regions with longer dwell times. Such scans, shown as insets in Figure 6, were recorded with energy steps of 0.2 eV and total dwell times of 1.0 s for F 1s and 0.7 s for N 1s, compared to 1 eV steps and 0.25 s total dwell times for the survey scan in Figure 5 and Figure 6. As a result, the standard deviations in the peak areas using Eq. (6) of Part 1 were reduced to 4 % (with $N_P = 36$ and $n_S = 0.53$) for the F 1s peak and to 9 % (with $N_P = 41$ and $n_S = 0.66$) for the N 1s peak. (The optimal $n_S = 1$ could not be used because the energy ranges of the recorded spectra were not large enough. Since $0.5 < n_S < 1$, the resulting statistical uncertainties are within 5% of the minimum value.) Note that a sufficiently large number of photoelectron trajectories were simulated by SESSA that the statistical uncertainties of the peak areas derived from the simulated spectra can be neglected.

In addition to the statistical uncertainties in the determination of peak areas, there are two main sources of systematic uncertainty in the SESSA simulations. First, the areas of the F and N peaks of the simulated spectra of Figure 6 are directly proportional to the corresponding photoionization cross sections. Seah *et al*.[24] made an extensive comparison of measured XPS peak intensities for 46 elemental solids with calculated intensities and concluded that there was overall agreement for the peaks of most practical interest with a one-standard-deviation uncertainty of about 9 %. This result depended not only on the Scofield[17] photoionization cross sections used to calculate peak intensities but on other parameters and on the method used to remove the inelastic background from the spectra. The second source of systematic uncertainty in the amounts of F and N in the surface layer of our sample is the neglect of surface excitations and of shakeup or intrinsic excitations in the SESSA simulations. While there is no clear evidence of these structures in the measured survey spectrum of Figure 6, we need to consider the systematic uncertainty associated with the neglect of surface and shakeup excitations in SESSA that leads to an underestimate of the F and N coverages. That is, we would need to assume larger F and N coverages to give the same peak intensities as those shown in Figure 6. The largest shakeup or surface peak area that could be present but not detected (false negative) is the critical level defined by Currie as the coverage factor, k, times the statistical uncertainty.[25] The statistical uncertainty of a shakeup or surface peak is determined by Eq. (6) of Part 1 with the same

parameters used for the main peak but with zero intrinsic peak-area uncertainty ($\sigma_{A_P} = 0$). With these assumptions, we estimate that neglect of possible shakeup or surface peaks would introduce (k=1) systematic relative uncertainties of 19 % and 29 % for the peak areas of F and N, respectively, determined from the survey scans. Although the narrow scans were not wide enough to encompass any shakeup or surface peaks, the same method used for the survey scans provides upper bounds on the relative systematic uncertainties introduced by neglecting these features in SESSA: 4.2 % for F and 8.9 % for N. The quadrature sum of these values with the cross-section uncertainties gives one-standard-deviation relative systematic uncertainties for the amounts of F and N in the surface layer of 21 % and 31 %, respectively, for the survey scans and 9.9 % and 12.7 %, respectively, for the narrow scans.

In our second example, Figure 7 shows a wide-scan XPS spectrum (solid blue circles) of a MLM sample used at NIST in EUV-photoresist outgas tests which we designate as Sample B. The XPS measurements and simulations for this sample were performed under the same conditions as Sample A except that the analyzer axis was set to 50° and the incidence angle of x rays on the sample was 10° (both with respect to the sample normal). To account for the lower signal at this angle, 15 sweeps were performed, each with 0.25 s dwell time. This sample shows a weak Cl impurity peak and stronger O and Si peaks than those in Figure 5 that are believed to be due to oxidized silicon dust particles produced when the samples were cut from a larger wafer. We therefore included an outermost 0.25-nm SiO2 layer in our simulations. The solid red triangles in Figure 7 show a simulated spectrum for a sample consisting of a 0.25 nm layer of SiO_2 on 0.25 nm $CCl_{0.01}$, 0.25 nm C, 0.25 nm RuO_2, 3 nm Ru, 4.3 nm Si, and 3 nm Mo on a Si substrate. The resulting spectrum was multiplied by the transmission function of our instrument and normalized to the measured spectrum at a binding energy of 400 eV.

The measured and simulated spectra in Figure 7 are qualitatively similar, but, as with Figure 5, there are differences in the heights and shapes of the Ru peaks. The weak Cl peak, shown on an expanded scale in Figure 8, occurs on a background due to the other elements in the sample; however, the intensity of the simulated Cl peak did not vary significantly with changes in the C, RuO_2, and Ru film thicknesses. As with Figure 5, we only need rough matches of the peak intensities and inelastic backgrounds in Figure 7 to quantify the amount of Cl in the sample. Furthermore, we note that the absence of structure due to inelastic scattering on the low-kinetic-energy side of the Cl peak in Figure 8 indicates that the Cl is a surface or near-surface impurity, as for N and F in Figure 6. We also point out that SESSA does not simulate valence-band spectra and the inelastic backgrounds associated with photoemission from the valence band. This limitation is of no consequence here since the valence-band peaks in the measured spectra in Figure 5(b) and Figure 7(b) are weaker than then the nearby Ru 4p peaks. While possible inclusion of the inelastic background from valence-band photoemission in Figure 7(b) could improve the overall agreement between measured and simulated spectra, we are mainly interested in the

relative magnitudes of the Cl 2p peaks above their local backgrounds in the measured and simulated spectra.

As with the F 1s and N 1s peaks of Sample A, we used symmetric, semi-correlated endpoint averaging to determine linear backgrounds for the Cl 2p peaks in the measured survey and simulated spectra shown in Figure 8. Comparison of the measured and simulated background-subtracted peak areas indicated that the composition of the outermost 0.25 nm carbonaceous layer was $CCl_{0.027}$. This corresponds to a coverage of 0.020 ML assuming a van der Waals radius for Cl of 0.175 nm. The relative statistical uncertainty of this result was estimated to be 13 % using Eq. (6) of Part 1 with $N_P = 12$. We estimate the systematic uncertainty of the Cl 2p photoionization cross section to be about 9 %,[24] as before, and the uncertainty associated with the neglect of surface and shakeup excitations to be about 13 %. The combined one-standard-deviation systematic uncertainty is then 16 %, and the total uncertainty in the amount of surface Cl is 21 %.

Our estimates of the amounts of surface impurities on our Samples A and B are summarized in the fourth column of Table 1 together with their statistical and total (quadrature sum of systematic and statistical) relative uncertainties in the fifth and sixth columns, respectively. As defined in Part 1 of this work and in Currie[25,26], the achievable detection limit for peak area is twice[†] the $k = 1$ statistical uncertainty of the background-subtracted peak area in the limit of zero peak area. Since our measured peaks are much smaller than the background signal, the contribution of the intrinsic variance of the peak area to the statistical uncertainties in column five is negligible, so the detection limits in units of ML given in column seven are simply twice the product of columns four and five. Note that the resulting detection limits are consistent with the size of the peaks displayed in the various spectra in Figures 6 and 8. (E.g., the F 1s peaks in the survey and narrow scans are factors of 2.7 and 12, respectively, above the predicted detection limits.)

Discussion

Our procedure for determining the amounts of N, F, and Cl impurities in our samples depends on knowledge of the location of these impurities. By comparison with control samples that were not exposed to resist outgassing, it was reasonable to assume that these impurities did

[†] The factor of two follows from normally distributed errors under the condition that the probabilities for *both* false positives *and* false negatives are equal and given by one minus the integral of the standard normal distribution from 0 to k+1.

in fact result from resist outgassing and that the detected carbon resulted from exposure of the MLM samples to the atmosphere following cleaning by atomic H. We note that it would also have been reasonable to include some oxygen in the surface layer for our simulations, but this did not appear to be necessary (i.e., the O 1s peak in the survey spectra could be attributed to the RuO_2 layer for Sample A in Figure 5 and to this layer and the outermost SiO_2 layer for Sample B in Figure 7). We were able to confirm that the N, F, and Cl impurities were at or near the surfaces of the MLM samples from the absence of detectable inelastic-scattering features in the measured spectra, as shown in Figure 6 and Figure 8.[22,23]

Shard[27] recently published calculations of XPS detection limits for more than 6000 binary systems in which an impurity element was assumed to be distributed homogeneously in a matrix of another element. His calculations were based on reasonable estimates of the background intensity due to the matrix for the impurity peak of interest and statistical uncertainties for determination of the peak area. Shard's results indicated that the detection limits for his specified measurement conditions could vary between about 0.003 atomic percent and 10 atomic percent for a trace element in a matrix of another elemental solid. Shard's results were presented as charts for XPS with Mg and Al Kα X-rays in which colors were used to distinguish the calculated detection limits in broad ranges, typically with factors of three between the detection limits in neighboring ranges.

Shard suggested that his XPS detection limits for an impurity in a matrix could be extended to the case of an impurity surface layer on a substrate of the matrix material. He estimated that the minimum average thickness, t_{DL}, of a surface species on a substrate of another material could be related to the corresponding bulk detection limit for that species, C_{DL}, in a matrix of the substrate material by

$$t_{DL} = L\, C_{DL}/100, \qquad (3)$$

where C_{DL} is expressed in atomic percent. The term L in Eq. (3) was described as the "attenuation length."[27]

Although Eq. (3) is useful for making rough estimates of detection limits for a surface species, it has some shortcomings. First, there was no formal derivation of Eq. (3). Second, an "attenuation length" is not a well-defined material parameter as implicitly assumed by Shard. Technical Committee 201 on Surface Chemical Analysis of the International Organization for Standardization has deprecated use of "attenuation length" and recommended instead the use of a newer term, the "effective attenuation length" (EAL) that is defined in the Appendix. The EAL is not a material parameter with a well-defined value for a particular material and electron energy (e.g., like the IMFP), and it is thus not clear how to determine the parameter L in Eq. (3).

Finally, another limitation of Eq. (3) is that t_{DL} does not depend on the average emission angle of photoelectrons emitted from the surface.

We now consider two alternative approaches for estimating detection limits for surface impurities. Our first approach is to consider a simple model for estimating the photoelectron intensity, I, from an element in a thin elemental film of thickness t on a planar substrate of another element:[10]

$$I = I_0\left[1 - e^{-t/(\lambda \cos \alpha)}\right], \quad (4)$$

where λ is the IMFP of film photoelectrons in the film, α is the average emission angle of the photoelectrons with respect to the surface normal, and I_0 is the photoelectron intensity from a thick film (with $t \gg \lambda$). Equation (4) was derived with the assumption that the effects of elastic scattering of the photoelectrons could be neglected.

We now use Eq. (4) to determine the film thickness, t_{DL}, that gives a photoelectron intensity $I_{DL} = I_0 C_{DL}/100$ where C_{DL} is the bulk detection limit (expressed in atomic percent) for the thin-film element in a matrix of the substrate elemental material. Since C_{DL} from Shard's calculations is always less than about 10 atomic percent,[27] t_{DL} will typically be much less than λ, and we then have

$$t_{DL} = \lambda \cos \alpha \, C_{DL}/100. \quad (5)$$

Equation (5) is obviously very similar to Eq. (3). Apart from the missing $\cos \alpha$ factor in Eq. (3), the equations would be identical if $L = \lambda$. Alternatively, Eq. (5) could be regarded as the defining equation by which the EAL in Eq. (3) (with the additional $\cos \alpha$ factor) could correct Eq. (5) for the effects of elastic scattering. This approach would be reasonable except for the fact that there is no known source of EAL data that could be generally used in Eq. (3). There are many sources of EAL data that can be used to describe the attenuation of substrate photoelectrons by an overlayer film but these data cannot be assumed to be valid for use in Eq. (3).

We now consider use of Eq. (5) for the example cases shown in Figure 5 and Figure 6 of N and F as surface species on the thick Ru layer comprising Sample A. From Figure 5 of Shard[27], the detection limits for N and F atoms in a Ru matrix are predicted to be 0.8 and 0.4 atomic percent, respectively, for the conditions used by Shard. We use Shard's Eq. (15) to scale these values to account for the different instrumental performance (magnitude of Ag $3d_{5/2}$ peak) and operational mode (energy step size and dwell time) of our measurements. Although we did not directly measure the Ag $3d_{5/2}$ peak, we estimate its magnitude to be 2.7×10^6 counts/second eV from a measurement of the Au $4d_{(5/2+3/2)}$ peak area times the ratio of relative sensitivity factors for Ag $3d_{5/2}$ and Au $4d_{(5/2+3/2)}$. (The Au measurement was only performed for the acquisition conditions of Sample A, with the detector axis normal to surface; therefore, we could not compare Shard's

predictions to our measurement of Cl on Sample B, which was performed at a detector angle of 50°.) We then multiply the detection limit from Shard's Eq. (15) by 4.9/9 to use the more accurate value of 4.9 $\sqrt{\text{eV}}$ for Shard's symbol of κ which is the proportionality factor between the peak area at the detection limit and the statistical uncertainty of the background signal divided by the square root of the energy step size. (The higher value of 9 $\sqrt{\text{eV}}$ suggested by Shard neglects the correlation between the background and peak areas. The lower value used here is the result of Eq. (6) of Part 1 which includes this correlation.)

With these adjustments, the $k = 1$ detection limits predicted by Shard for N and F in a matrix of Ru are 0.53 and 0.27 atomic percent, respectively , for the measurement conditions of the survey spectrum in Figure 5, and 0.14 and 0.059 atomic percent, respectively, for the measurement conditions of the narrow scan in the insets of Figure 6. We use these values for C_{DL} in Eq. (5) to find the equivalent detection limits, t_{DL}, as thicknesses of N or F films on a Ru substrate. We then convert these thicknesses to coverages by dividing by twice the van der Waals radius, which was taken to be 0.155 nm for N and 0.147 nm for F. Assuming that the IMFPs of N 1s and F 1s photoelectrons from the films can be estimated from the TPP-2M predictive formula of Tanuma *et al*.[21], the surface-layer detection limits predicted by Shard's estimates and Eq. (5) for N and F are 0.055 ML and 0.023 ML, respectively, for our survey scans and 0.015 ML and 0.0051 ML, respectively, for our narrow scans.

We now evaluate a second approach using SESSA for determining amounts of surface impurities from the XPS detection limits calculated by Shard. We followed the procedure of Powell *et al*.[28] in which a SESSA simulation is made first for a sample consisting of a matrix element (assumed here to be Ru) and an impurity element (here assumed to be N or F representative of the surface impurities on our Sample A). Independent SESSA simulations were made for homogeneous solids RuN_x and RuF_y using the stoichiometries (x and y) equal to the matrix detection limits predicted by Shard and determined above for both acquisition conditions used to measure Sample A (x=0.0053, y=0.0027 and x=0.0014, y=0.00059 for the survey and narrow scans, respectively). We then performed a second series of SESSA simulations with the same instrumental conditions but in which the N or F is present as a surface film on a Ru substrate. The thickness of the N or F film was varied until the partial intensity of the N 1s or F 1s photoelectrons matched the corresponding intensity from the first SESSA simulation (within 2 %). These simulations led to detection limits for N and F present as impurity films of 0.032 ML and 0.013 ML, respectively, for the survey scan conditions of Sample A, and 0.0080 ML and 0.0029 ML, respectively, for the narrow scans. (The same van der Waals radii as above were used here to convert from thickness to coverage.) We have thus used SESSA to convert an XPS detection limit for a minor species in a homogeneous solid (e.g., as estimated by Shard[27]) to the corresponding XPS detection limit for that species present as a thin film on the chosen substrate.

This approach can also be used to determine the XPS detection limit for the chosen impurity species present as a buried layer in a given solid.[28]

Table 2 summarizes the XPS detection limits for N and F as surface layers on a Ru substrate derived from Shard's XPS detection limits for binary matrices using Eq. (5) and using SESSA. Values are given for acquisition conditions of the survey and narrow spectra as described above. We see that the detection limits determined using SESSA are between 10 % and 30 % larger than the values in column seven of Table 1, while the limits predicted by Eq. (5) are 2.0 to 2.2 times larger than the Table 1 values. The larger discrepancy of the latter results are likely due to the inherent limitations of Eq. (5). First, we have neglected the effects of elastic scattering in both Eqs. (4) and (5). Second, we note that the values of C_{DL} calculated by Shard were probably for XPS with photoelectrons emitted normally from each considered material. Since C_{DL} values will change with emission angle, it would be incorrect to infer from Eq. (5) that smaller detection limits could be obtained by increasing α. Nevertheless, previous SESSA simulations (that included elastic-scattering effects) for emission angles of 0° and 55° have shown that values of $t_{DL}/\cos\alpha$ were independent of α for W on a Ru substrate and for Ru on a W substrate.[28] Additional validation beyond the comparisons between Tables 1 and 2 are needed to determine the accuracy and ultimate usefulness of Eq. (5).

SUMMARY

We discussed common sources of systematic uncertainties and methods for absolute quantification associated with the analysis of trace levels of surface contamination on multilayer structures by XPS. The problem was framed according to the needs of EUV Lithography resist-qualification tests, but the methods and conclusions summarized below are applicable to a wide variety of applications.

1. We discussed the ambiguity of relative atomic concentration used frequently for quantification of trace elements on multi-layer EUV optic samples, and demonstrated that the relative concentration of S, P, or halogens (or other trace elements) on a Ru surface could be dramatically overestimated if the contribution of the C 1s peak was not included in the analysis of the Ru 3d region.
2. We showed that absolute coverages of surface impurities on samples could be estimated from comparisons of measured XPS spectra with simulated spectra from the NIST SESSA database. The primary contributions to the statistical and systematic uncertainties of these estimates were also described, and the corresponding detection limits were evaluated. Our procedure could be similarly used for impurities suspected to be located in various layers of a multilayered material.

3. We pointed out that the Shard[27] procedure for estimating XPS detection limits for adsorbates or impurities on surfaces is based on an unsatisfactorily defined "attenuation length." We proposed an alternative procedure that uses an inelastic mean free path. We also described a method involving the use of SESSA to compare photoelectron intensities from a dilute impurity in an elemental solid (with a concentration set by the bulk XPS detection limits reported by Shard) to the corresponding intensities for that impurity as a surface film on the elemental solid. Both approaches provide a useful means for converting an XPS detection limit for a bulk solid to the corresponding detection limit for a surface film.

Acknowledgment

We thank Dr. A. G. Shard for helpful comments.

Appendix

The effective attenuation length has been defined as the "parameter which, when introduced in place of the inelastic mean free path (IMFP) into an expression derived for Auger electron spectroscopy (AES) and XPS on the assumption that elastic-scattering effects are negligible for a given quantitative application, will correct that expression for elastic-scattering effects."[29] Two explanatory Notes accompanying this definition are currently being revised with the following proposed text:

(1) The effective attenuation length can have different values for different quantitative applications of AES and XPS. However, the most common use of effective attenuation length is in the determination of the thicknesses of overlayer films on flat substrates from measurements of the changes of overlayer and substrate Auger-electron or photoelectron signal intensities as a function of film thickness or of electron emission angle. For emission angles of up to about 60° (with respect to the surface normal), it is often satisfactory to use a single value of this parameter. For larger emission angles, the effective attenuation length can depend on this angle. Effective attenuation lengths have also been used in equations for determining the shell thicknesses of core-shell nanoparticles and for quantitative analysis (to describe the changes in AES and XPS signal intensities due to elastic scattering).

(2) Since there are different uses of this term, it is recommended that users specify clearly the particular quantitative application and the definition of the parameter for that application (e.g. by giving a formula or by providing a reference to a particular source). Effective attenuation lengths developed for one application should not be used for another application unless this usage has been validated.

REFERENCES

[1] I Pollentier, A Tirumala Venkata, R Gronheid, *Proc SPIE, Extreme Ultraviolet (EUV) Lithography V* **2014** ; 9048 , 90481B–90481B–9.

[2] TE Madey, NS Faradzhev, BV Yakshinskiy, NV Edwards, *Applied Surface Science* **2006** ; 253 , 1691–708.

[3] R Garg, A Wüest, E Gullikson, S Bajt, G Denbeaux, *Proc SPIE, Emerging Lithographic Technologies XII* **2008** ; 6921 , 692136-692136–8.

[4] SB Hill, NV Faradzhev, CJ Powell, *Surface and Interface Analysis* **2017** ; 49, 1187-1205.

[5] WSM Werner, W Smekal, CJ Powell, NIST Database for the Simulation of Electron Spectra for Surface Analysis, Version 1.3, Standard Reference Data Program Database 100 2011; see http://www.nist.gov/srd/nist100.cfm

[6] W Smekal, WSM Werner, CJ Powell, *Surf Interface Anal* **2005** ; 37 , 1059–67.

[7] SB Hill, NS Faradzhev, C Tarrio, TB Lucatorto, TE Madey, BV Yakshinskiy, et al., *Proc SPIE, Emerging Lithographic Technologies XII* **2008** ; 6921 , 692117-692117–11.

[8] H Over, YB He, A Farkas, G Mellau, C Korte, M Knapp, et al., *Journal of Vacuum Science & Technology B: Microelectronics and Nanometer Structures Processing, Measurement, and Phenomena* **2007** ; 25 , 1123–38.

[9] Commercial products are identified to specify the experimental conditions. This identification does not imply that the products are endorsed or recommended by the National Institute of Standards and Technology or that they are necessarily the most suitable for the purposes described.

[10] CJ Powell, A Jablonski, *Journal of Electron Spectroscopy and Related Phenomena* **2010** ; 178–179 , 331–46.

[11] WM Haynes, In: Handbook of chemistry and physics. 95th ed. CRC Press, Boca Raton, 2014:9–49.

[12] CJ Powell, JM Conny, *Surf Interface Anal* **2009** ; 41 , 269–94.

[13] JM Conny, CJ Powell, LA Currie, *Surf Interface Anal* **1998** ; 26 , 939–56.

[14] JM Conny, CJ Powell, *Surf Interface Anal* **2000** ; 29 , 444–59.

[15] JM Conny, CJ Powell, *Surf Interface Anal* **2000** ; 29 , 856–72.

[16] CasaXPS software, Version 2.3.14, N Fairley; see http://www.casaxps.com

[17] JH Scofield, *Journal of Electron Spectroscopy and Related Phenomena* **1976** ; 8 , 129–37.

[18] RF Reilman, A Msezane, ST Manson, *Journal of Electron Spectroscopy and Related Phenomena* **1976** ; 8 , 389–94.

[19] WSM Werner, (Unpublished data)

[20] S Tanuma, CJ Powell, DR Penn, *Surf Interface Anal* **1993** ; 20 , 77–89.

[21] S Tanuma, CJ Powell, DR Penn, *Surf Interface Anal* **1994** ; 21 , 165–76.

[22] S Tougaard, *Journal of Vacuum Science & Technology A: Vacuum, Surfaces, and Films* **1996** ; 14 , 1415–23.

[23] CJ Powell, S Tougaard, WSM Werner, W Smekal, *Journal of Vacuum Science & Technology A: Vacuum, Surfaces, and Films* **2013** ; 31 , 021402.

[24] MP Seah, IS Gilmore, SJ Spencer, *Journal of Electron Spectroscopy and Related Phenomena* **2001** ; 120 , 93–111.

[25] LA Currie, *Analytical chemistry* **1968** ; 40 , 586–593.

[26] LA Currie, *Analytica Chimica Acta* **1999** ; 391 , 127–134.

[27] AG Shard, *Surface and Interface Analysis* **2014** ; 46 , 175–85.

[28] CJ Powell, WSM Werner, W Smekal, *Journal of Vacuum Science & Technology A: Vacuum, Surfaces, and Films* **2014** ; 32 , 050603.

[29] *ISO 18115-1, Surface Chemical Analysis – Vocabulary, Part 1 – General Terms and Terms Used in Spectroscopy* International Organization for Standardization, Geneva, **2013**.

Table 1. Summary of estimates of amounts of each element present as surface impurities on Samples A and B using SESSA simulations as well as their statistical and total relative uncertainties. Also shown are the achievable detection limits determined by the methods of Part 1 of this work[4] (with coverage factor $k = 1$) for our XPS measurement conditions.

Sample	Element	Measured spectrum	Amount (ML)	Relative statistical uncertainty	Total relative uncertainty	Achievable Detection limit (ML)
A	F	Survey	0.027	19 %	29 %	0.010
A	F	Narrow	0.027	4.2 %	11 %	0.0023
A	N	Survey	0.043	29 %	42 %	0.025
A	N	Narrow	0.043	9.0 %	16 %	0.0076
B	Cl	Survey	0.020	13 %	21 %	0.0051

Table 2. Estimated XPS detection limits (with coverage factor $k = 1$) for F and N as surface impurities on Ru derived from Shard's data[27] using Eq. (5) and SESSA simulations.

Sample	Surface Impurity	Measured Spectrum	Detection Limit from Eq. (5) (ML)	Detection Limit from SESSA (ML)
A	F	Survey	0.023	0.013
A	F	Narrow	0.0051	0.0029
A	N	Survey	0.055	0.032
A	N	Narrow	0.015	0.0083

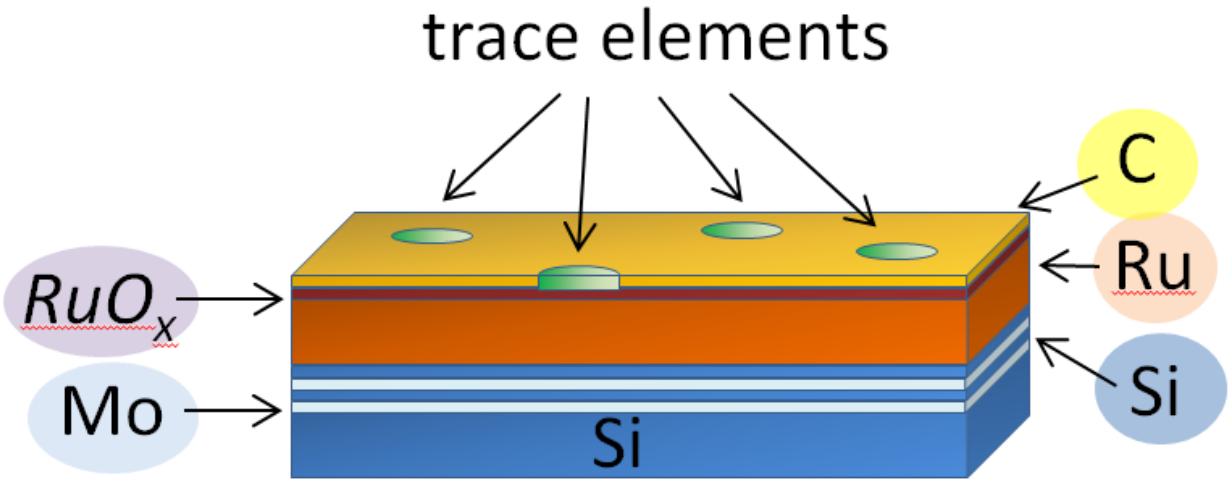

Figure 1 Sketch of surface model of multilayer mirror used in calculations for trace elements: MoSi bilayers deposited on a Si substrate and coated with a Ru polycrystalline film. This film has a native oxide ($RuO_{x\cong2}$) layer with a thickness of 0.5 nm. The trace element is located on top of this oxide film and covered with a thin hydrocarbon layer resulting from air exposure (simulated by a thin layer of carbon).

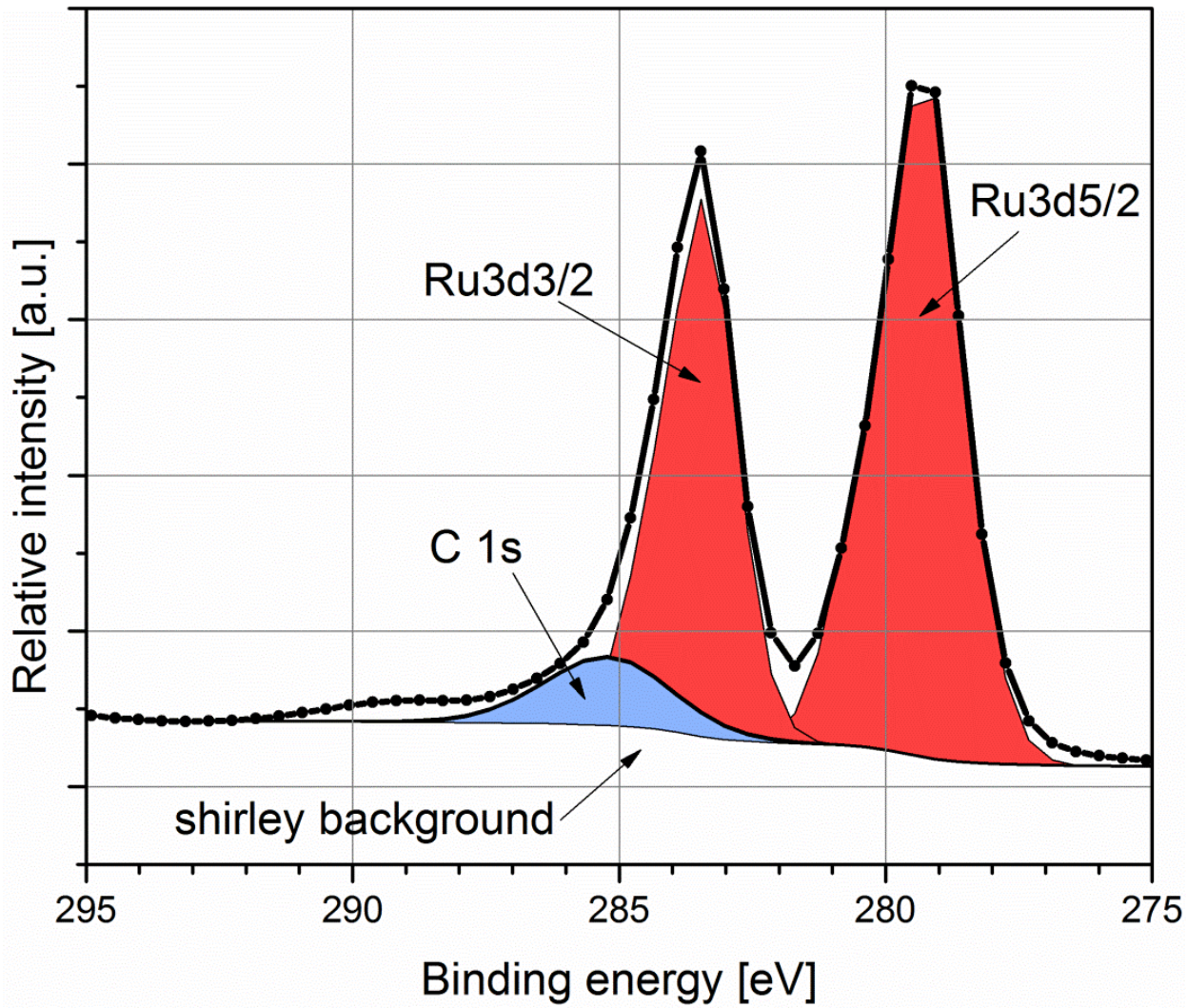

Figure 2 Simulated spectrum from SESSA in arbitrary units (a.u.) showing the Ru 3d/C 1s region for a 30 nm Ru film with a 0.5 nm RuO_2 layer covered by 0.07 nm of S and 0.5 nm of C. The spectrum was obtained with the analyzer axis set to 50° with respect to the surface normal and using instrumental parameters of the Kratos Axis Ultra spectrometer.[9] SESSA provides the principal spectra for the C 1s, Ru $3d_{3/2}$, and Ru $3d_{5/2}$ components (thin curves without symbols with shaded areas) as well as the total spectrum (thick curve with symbols). The assumed Shirley background is also shown (lower-bound thin black curve).

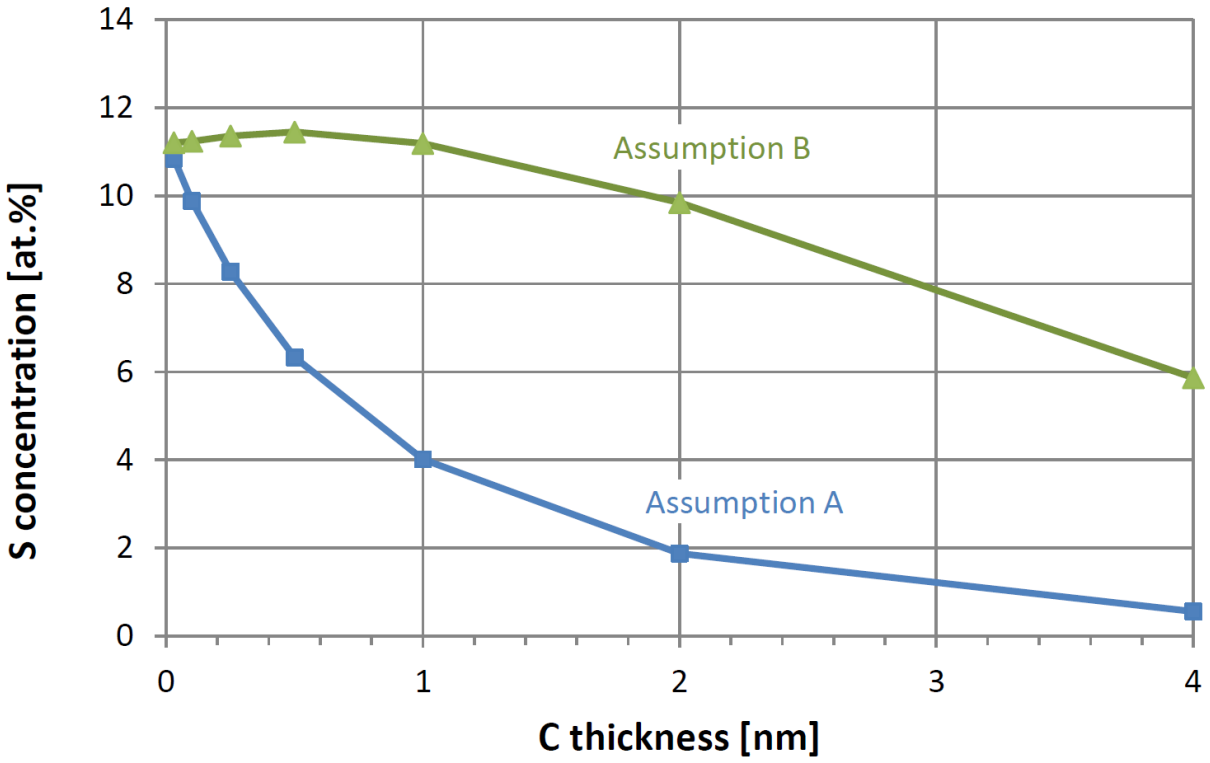

Figure 3 Relative atomic concentrations expressed in atomic percent (at. %) of sulfur on Ru as a function of C overlayer thickness as described in the text. The 30 nm Ru film has a 0.5 nm native oxide film covered with 0.07 nm (0.19 ML) of sulfur and a carbon layer of varying thicknesses. The blue curves (squares) result from Assumption A in which the Ru 3d and C 1s components were each fit independently, while the green curves (triangles) result from Assumption B in which the spectrum was fit to the Ru 3d components only, and the C 1s contribution was neglected.

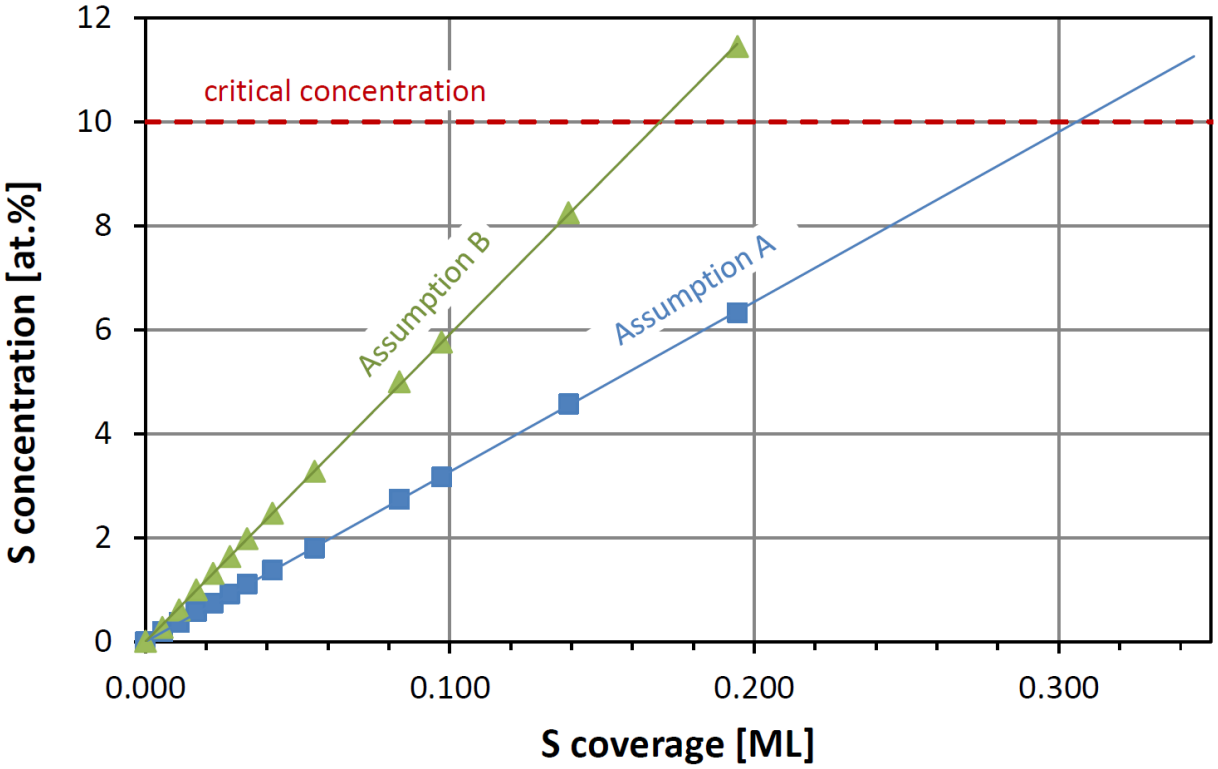

Figure 4 Relative atomic concentration of sulfur calculated as a function of S surface coverage expressed in monolayers (ML) for an assumed homogeneous sample consisting of a 30 nm Ru film, a 0.5 nm RuO_2 film, the S film, and a 0.5 nm layer of carbon. The sulfur coverage was calculated by assuming 1 ML is equal to twice the van der Waals radius of S, taken to be 0.18 nm. The results were obtained from photoelectron spectra simulated by SESSA for our instrumental conditions. As in Figure 3, the blue squares and green triangles depict results from our use of Assumptions A and B, respectively, for which the C 1s peak was included or excluded in fits of the Ru 3d/C 1s region of the spectrum. The solid lines indicate linear fits through the origin for each group of points. The horizontal dashed line indicates a hypothetical critical S atomic concentration (e.g., the upper limit for acceptable outgassing of an EUV resist).

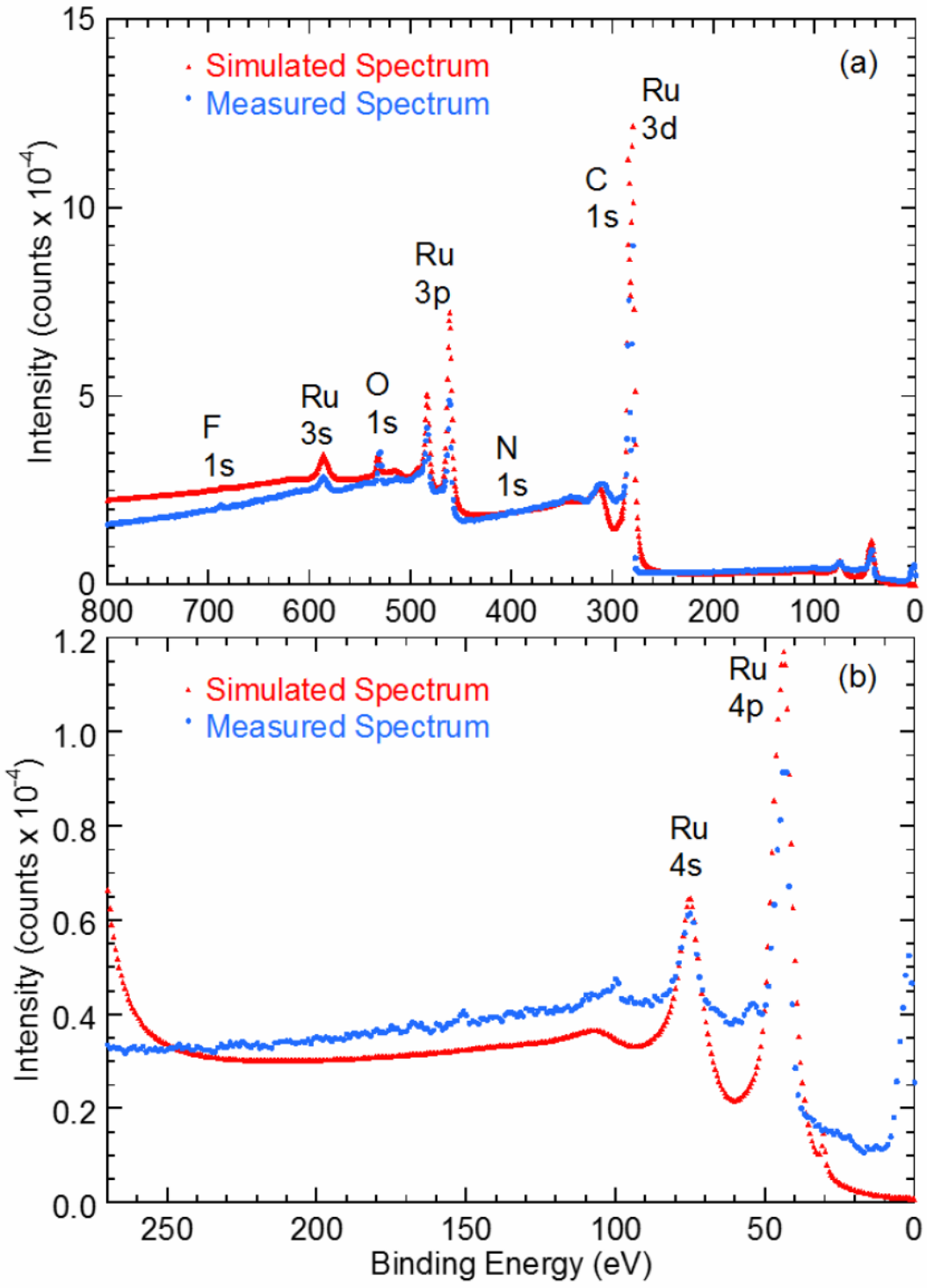

Figure 5 (a) Comparison of measured (solid blue circles) and simulated (solid red triangles) XPS spectra for Sample A; see text for details. The ordinate scale is the total number of measured photoelectrons at each energy. The simulated spectrum was normalized to the measured spectrum at a binding energy of 390 eV. (b) shows expanded low-energy region of (a).

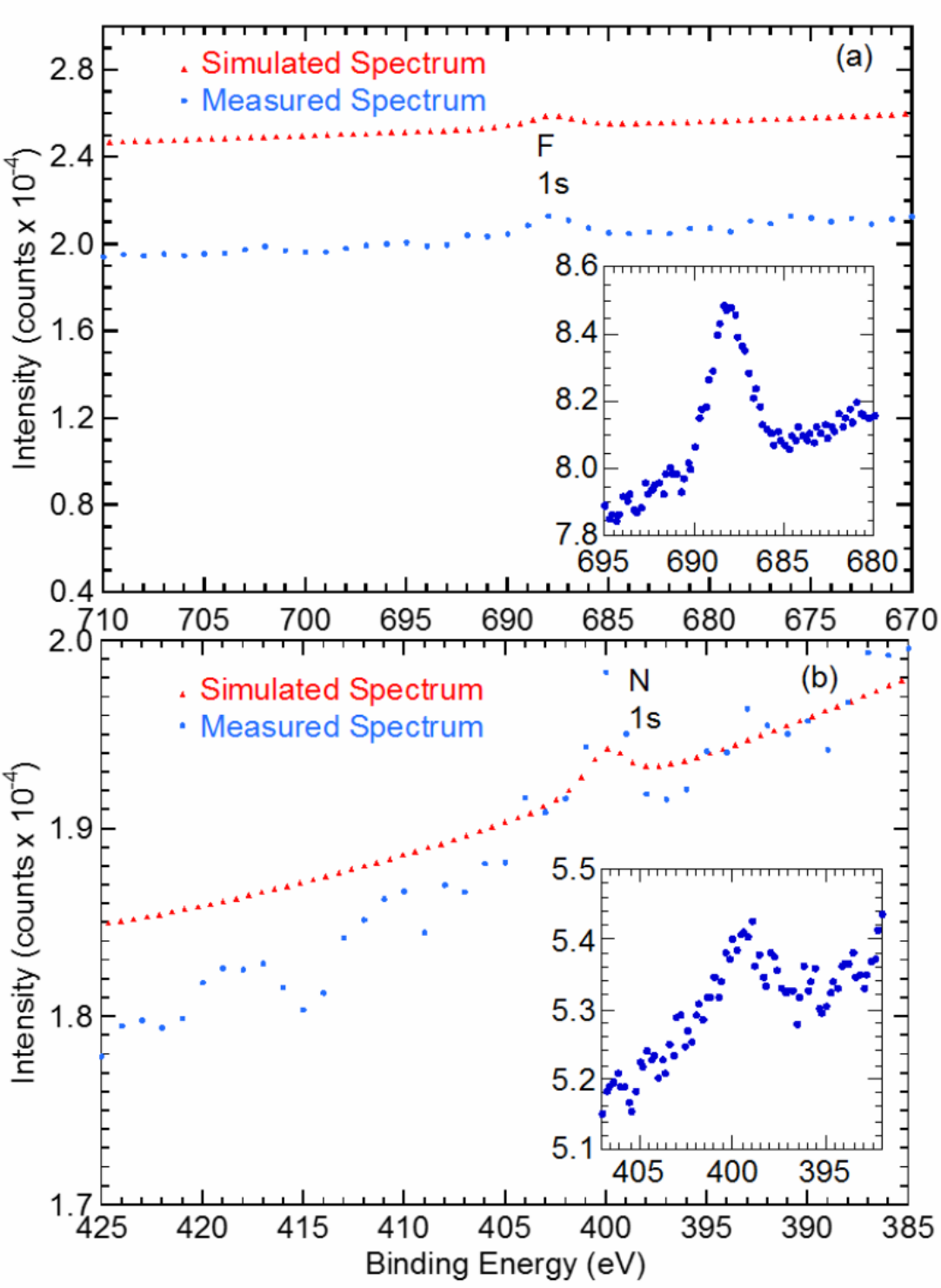

Figure 6 Comparison of measured (solid blue circles) and simulated (solid red triangles) XPS spectra for Sample A in the regions of (a) the F 1s peak and (b) the N 1s peak. The insets show narrow-scan spectra for the F 1s and N 1s peaks; see text for details.

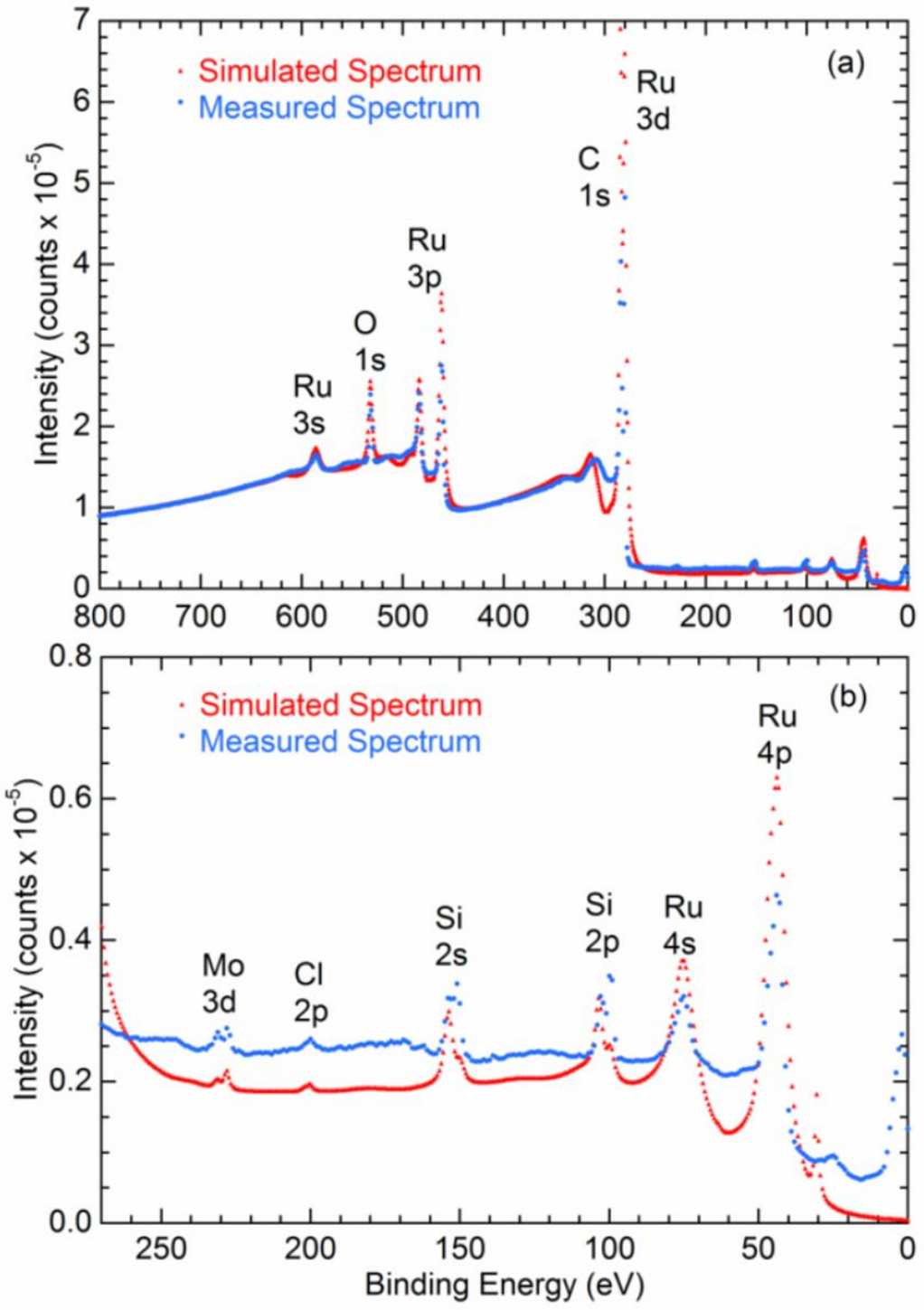

Figure 7 (a) Comparison of measured (solid blue circles) and simulated (solid red triangles) XPS spectra for Sample B; see text for details. The ordinate scale is the total number of measured photoelectrons at each energy. The simulated spectrum was normalized to the measured spectrum at a binding energy of 400 eV. (b) shows expanded low-energy region of (a).

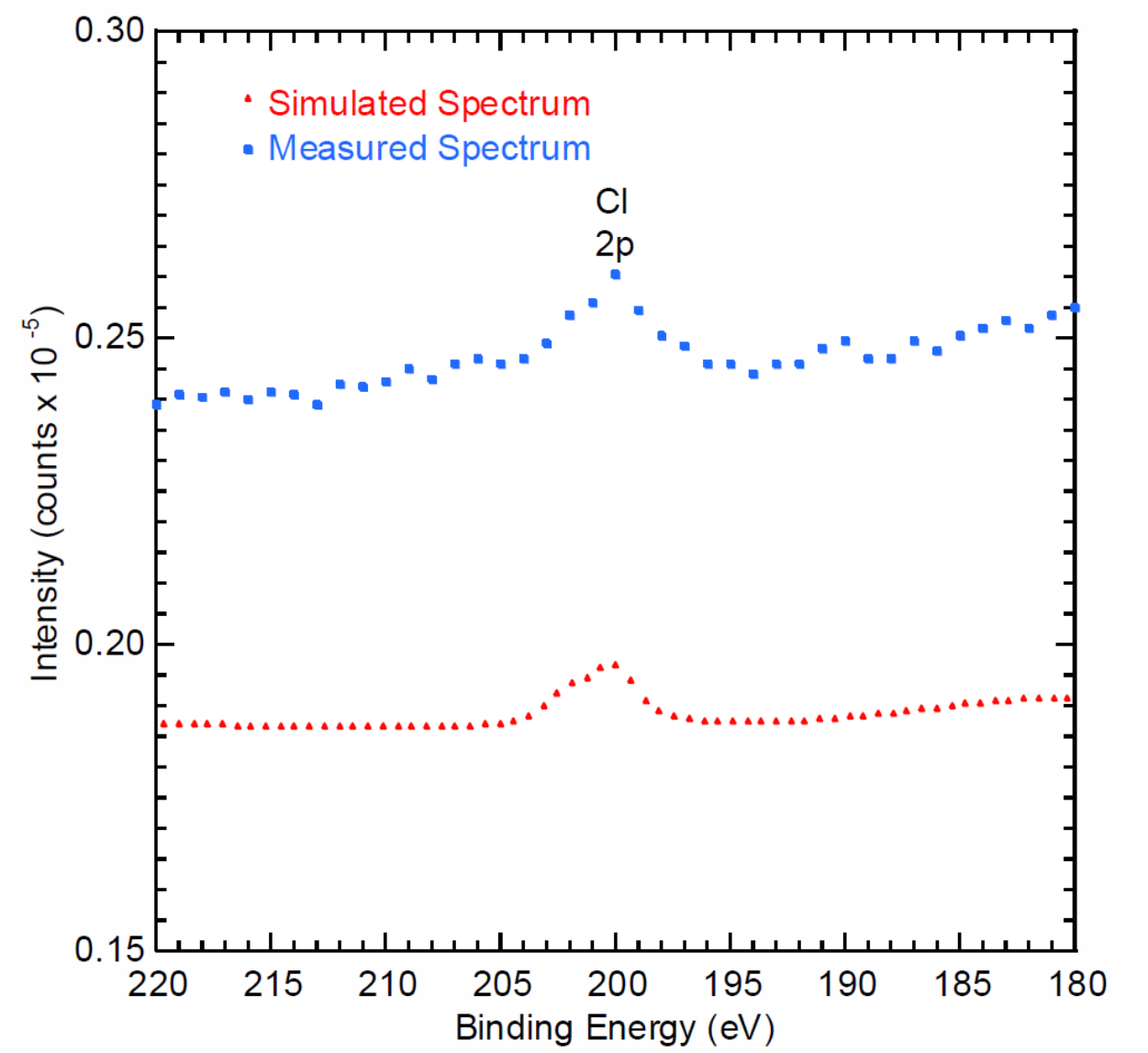

Figure 8 Comparison of measured (solid blue circles) and simulated (solid red triangles) XPS spectra for Sample B in the region of the Cl 2p peak.